Biophysical Modeling of Endolymph Transport During Inner Ear Development

Biophysical Modeling of Endolymph Transport During Inner Ear Development.

Kishore Mosaliganti

A Thesis in the Field of Biotechnology

for the Degree of Master of Liberal Arts in Extension Studies

Harvard University

May 2018

Abstract

The goal of this work was to investigate the biophysical mechanisms underlying fluid transport across a single-cell epithelium in the context of inner ear development. The primordial inner ear grows as a fluid-filled spherical shell, called as the otic vesicle, to form complex sub-organs necessary for hearing and balance. The luminal fluid, called endolymph, is tightly regulated in terms of its composition and volume throughout development and whose dysregulation leads to hearing and balance disorders. Previous work showed that fluid transport creates hydrostatic pressure in the luminal cavity that feeds back to inhibit fluid transport and regulate vesicle growth rates. As a first step to linking how pressure affects fluid transport mechanisms, this study focused on the origin of the fluid, the path taken, and the biophysical mechanism underlying its transport into the luminal cavity. In order to distinguish whether intracellular fluid or fluid external to the inner ear (perilymph) contributes to transport, quantitative imaging techniques were used with small fluorescent tracer dyes. 3D+*time* visualizations of localization patterns provide direct evidence of the path of endolymph. The tracer dye highlighted a paracellular pathway across basal junctions of cells, lateral spaces between adjacent cells, and across apical junctions. To rule out the possibility of different paths taken by dye and fluid, several mathematical models of dye transport were evaluated by accounting for geometry and growth dynamics of the vesicle. Data from experimental perturbations were used to validate model predictions to prove that tracer dye movement is advectively coupled to fluid movement.

Dedication

In the hope that this work may in some way contribute to the understanding of the intricate biological mechanisms that may one day contribute to the development of cures and therapies, this is dedicated to all basic science researchers.

Acknowledgments

I would like to express my sincere gratitude to my research advisor and postdoc mentor Professor Sean Megason for his wisdom, patience, and guidance during this project. To my thesis director Dr. Steve Denkin for closely working with me on the thesis proposal and reviewing the final thesis. I would also like thank Harvard University for creating resources for continued learning via The Extension School, the dedicated faculty and part-time instructors who went above and beyond to teach with passion, and members of the Megason Lab and Department of Systems Biology, Harvard Medical School. Finally, I am also thankful to the love and support I receive on a daily basis from my many friends and family members.

Table of Contents

List of Figures

Chapter I.

Introduction

Early ear development confers vertebrate animals with a clarified sense of hearing and balance, and whose disruption leads to deafness, dizziness, and vertigo. Hearing is the process of converting a mechanical sound wave to an electrical signal for transmission to the brain. The ear organ facilitates this process and it consists of three chambers: outer, middle, and inner ear. The outer ear collects and transmits the signal and vibrates the ear drum membrane. The middle ear amplifies the mechanical signal and sends it to the inner ear. The inner ear consists of 3 semi-circular canals (scc) and a cochlea. The scc allows us to maintain balance while the cochlea allows us determine the acoustic properties of the sound wave. According to statistics compiled by the Statistics and Epidemiology division at the National Institute of Deafness and Other Communicable Disorders (NIDCD) from the 1999-2010 National Health and Nutrition Examination Survey (NHANES), approximately 15% of American adults (37.5 million) aged 18 and over report some trouble hearing (NIDCD, 2010). About 2 percent of adults aged 45 to 54 have disabling hearing loss. The rate increases to 8.5 percent for adults aged 55 to 64. Nearly 25 percent of those aged 65 to 74 and 50 percent of those who are 75 and older have disabling hearing loss. While most cases arise from a complex combination of genetics, environment, and aging, there are extreme cases for which the cause is congenital. About 2 to 3 out of every 1,000 children in the United States are born with a detectable level of hearing loss in one or both ears (CDC, 2003). The development of therapeutic interventions and cures involves resolving the nature of their origins in the

embryo (Bartel-Friedrich & Wulke, 2007, Yin et al., 2011). Thus, understanding inner ear development is an important prerequisite to understanding and curing hearing and balance disorders.

Studying Organ Development to Treat Ear Disorders

Understanding the principles of organogenesis, the self-organized process by which organs are robustly constructed, is one of the central goals of developmental science. Deciphering these principles will directly facilitate efforts to build organs in-vitro using stem-cell therapies, a major frontier of current research. Organogenesis involves three intertwined biological processes known as morphogenesis, patterning, and growth. Morphogenesis refers to the process by which tissues are bent and molded to achieve the right form. It is believed that the genome encodes morphogenetic circuits that direct progenitor cells to proliferate, rearrange, and change shape in a dynamic manner to control tissue size and shape. Patterning refers to the process of building the right types of cells at the right places. Patterning circuits create different cellular identities using positional information, cell lineage history, and extracellular signals to drive intracellular gene expression. Growth involves the process of changing tissue size so the organ is constructed to the right size to facilitate its function. By virtue of being a small, self-contained and fluid-filled organ, the developing inner ear serves as a model-system for the study of morphogenesis and growth across an entire class of fluid-filled organs including the eyes, lung, gut, kidney, bladder, brain, Kupfers vesicle and vascular system. As in the case of the inner ear, these organs originate as small vesicles or tubes that undergo further morphogenesis and growth through tissue and fluid accumulation (Gin, Tanaka, & Brusch, 2010).

Zebrafish as a Model-System to Study Organogenesis

The zebrafish is particularly suited for studying biological processes involved in organ-formation *in vivo*. The zebrafish is a vertebrate and therefore it presents mechanisms very similar to the mouse and human model system. Hence, studies of zebrafish development are very relevant to other model-systems. Embryos develop *ex-utero* and therefore it can be easily observed, manipulated, and compared with each other. An adult fish can lay more than 200 eggs with the same genetic background on a weekly basis. The availability of such large numbers of embryos facilitates the study of noise and natural variation in development. Zebrafish embryos also develop relatively rapidly. Compared to large gestational times in humans and mice, the zebrafish body plan including most organs such as the somites, eyes, ear, and heart are laid out in less than 3 days post-fertilization (Kimmel, 1995). Zebrafish embryos are transparent and so one can use fluorescent reporters of gene and protein expression in conjunction with powerful microscopy techniques (Megason, 2009). Furthermore, several experimental techniques, including mutant analysis, microinjection of mRNAs, morpholinos, and drugs, and engineering transgenesis in large numbers of embryos, can be applied to zebrafish.

These generation time and experimental accessibility of zebrafish embryos have allowed the isolation of numerous types of inner-ear mutants (Freter et al., 2008 and McCarroll et al., 2012). Although inner-ear development was originally studied in the frog (Brigande et al., 2000), mouse (Satoh et al., 2005), and chick systems (Lang et al., 2001 and Kil et al., 2001), the small, self-containing ear compartment in the zebrafish allows one to study it at single-cell resolution by using live imaging techniques (Sanchez-

Guardado et al., 2014). The project findings described here, while possible in the optically accessible zebrafish, would be impossible in the mouse or chicken or frog.

Inner ear development in the zebrafish

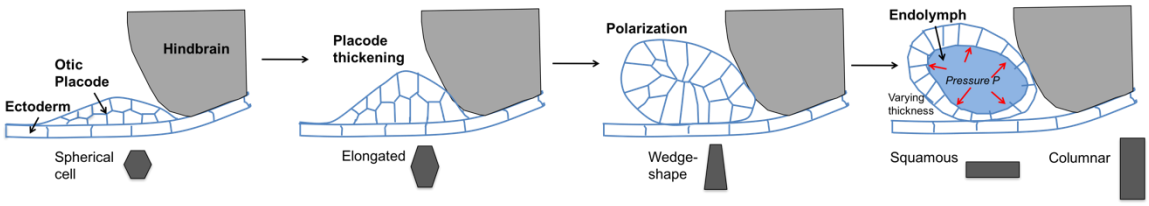

Figures 1: An illustration of otic vesicle formation in the zebrafish embryo

Between 12-45 hours post-fertilization (hpf), spherical-shaped cells from the otic placode elongate, divide, and rearrange into a polarized ball of epithelial tissue called the otic vesicle. Cells develop intercellular junctions and change into a wedge-shape. Cells transport fluid and increase in cell number to form endolymph and the otic vesicle grows to reach the right size and shape. Cells change from a columnar shape to a squamous shape (Mosaliganti et al., 2017).

The vertebrate inner ear develops from a thickening of embryonic ectoderm called the otic placode, located lateral to the hindbrain (Haddon & Lewis, 1996 and Whitfield, 2015 and Wu & Kelley, 2012) (Figure 1). Between 11-13 hpf, cells in the placode proliferate, elongate medially, and form two layers of cells. The layers of cells in the otic placode are induced, then epithelialize, and connect to form a hollow structure called the otic vesicle. At 16 hpf, cells secrete fluid from their apical membranes to form a lumen. The otic vesicle then inflates by increasing its tissue mass, as well as by continuing secretion of fluid, called as the endolymph. Between 18-48 hpf, the otic vesicle grows in size with rapid cell division and with lumen expanding. At about 48hpf, semi-circular

canal (scc) formation begins by in-growth of projections from the walls of the vesicle, which fuse to span the ear lumen. Subsequently, in addition to the scc, the otic vesicle further develops a complex topology consisting of the ampullae, saccule, utricule, and duct and sac.

Quantitative *3D+time* imaging of zebrafish inner ear

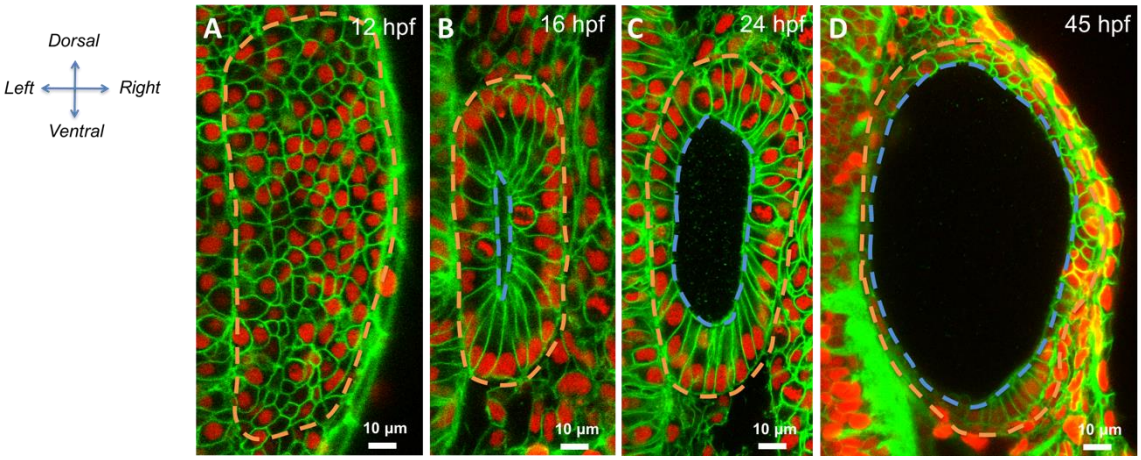

Figure 2. Confocal micrographs of otic vesicle development

(A) 12 hpf, (B) 16 hpf, (C) 24 hpf, and (D) 45 hpf (Mosaliganti et al., 2017). Orange and blue contours demarcate otic vesicle and luminal surfaces respectively. Embryos are double transgenic for highlighting membranes and nuclei (Tg(actb2:Hsa.H2B-tdTomato)^{hm25}; Tg(actb2:mem-citrine)^{hm26}).

In the last decade, advances in imaging technologies have led to the development of robust, integrated systems approaches to the study of biology. By using confocal, 2-photon, or light-sheet microscopy with cells expressing fluorescent reporters tagged to cell membranes and nuclei, one can obtain *3D+time* movies of development in live and intact embryos. This form of imaging, referred to as *in toto* imaging, reveals dynamic and

mechanistic information across a range of spatial scales, from sub-cellular to organ-level (Megason, 2009). At the tissue scale, one can quantify the size and shapes of organs and tissue compartments. At the level of cell domains, one can quantify collective cell behavior in terms of cell morphologies and packing arrangement within bulk tissue. Individual cells can be temporally tracked to reconstruct complete lineage histories and fate maps of organs. These quantifications provide insight into morphogenetic mechanisms that construct the organ. At a subcellular scale, one can explore patterning strategies, in terms of the network architecture, through the quantification of single-cell dynamics of gene and protein expression. Figure 2 shows an 2D *in toto* micrographs of the zebrafish inner ear during its development stages from placode induction, epithelialization, lumenization, and growth.

Image analysis challenges with *in toto* data

Given the large size and multidimensional nature of *in toto* datasets, highly specialized tools are required for image acquisition, data management, image analysis, and visualization. In a recent article, Elicieri and colleagues comprehensively reviewed the state-of-the-art open-source software platforms available for building an informatics pipeline (Elicieri 2012). The main tools relevant to this project are ImageJ (Collins, 2007), Fiji (Schindelin, 2012), and Gofigure2 (Xiong et al., 2014) for image analysis and visualization. For comprehensively quantifying cell behavior, the Megason Lab at Harvard Medical School have previously developed image-analysis algorithms for solving problems of registration, cell segmentation, cell tracking, and cell lineaging that can then be used in combination with these tools to provide visualizations of our data (Mosaliganti, 2012).

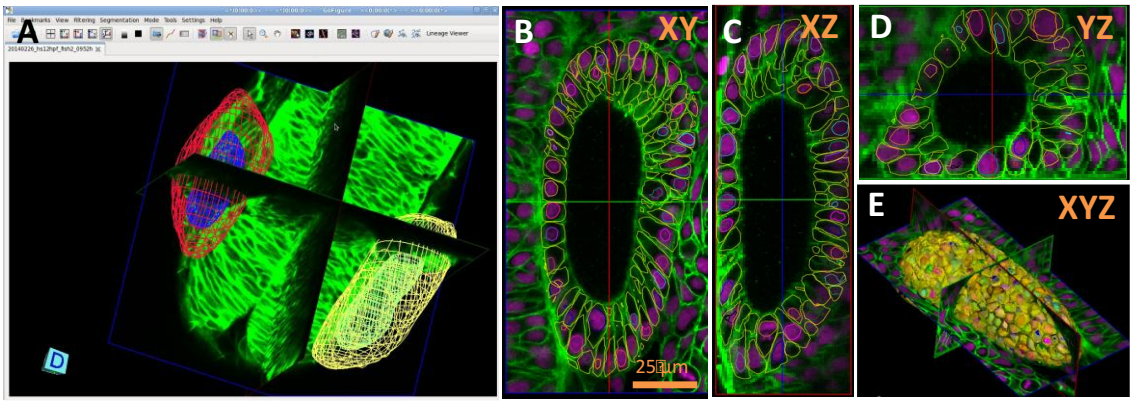

Figure 3. *In toto* image analysis using GoFigure2 software

(A) Organ size and shape can be semi-automatically or manually processed by placing 2D contours along image planes in the GoFigure2 software platform. The software reconstructs surfaces from contours and computes volumes and surface areas. In toto images can be automatically processed using membrane and nuclei segmentation algorithms for estimating cell numbers, cell shapes, and protein expression at a single-cell resolution. Using GoFigure2, an open-source software for visualization, editing, and integrative analysis of in toto data, the segmentation meshes and tracks can be visualized along orthogonal image planes as shown in (B) XY, (C) YZ, (D) XZ, and as (E) triplanar 3D view.

Otic Vesicle Growth from Fluid Flux

Despite the critical role of otic vesicle growth in generating future organs of the inner ear, the mechanisms underlying its morphogenesis and growth are mostly unknown. Recent work in the Megason Lab, Department of Systems Biology, HMS has focused on identifying a biophysical basis for growth control in the zebrafish inner ear (Mosaliganti et al., 2017).

The total vesicle volume was found to be a combination of the outer tissue shell and the endolypmph fluid in the luminal cavity. Quantification of the early growth dynamics showed that luminal inflation from fluid accumulation (referred as endolymph) dominates growth. Tissue growth from cell division was found to play a secondary role.

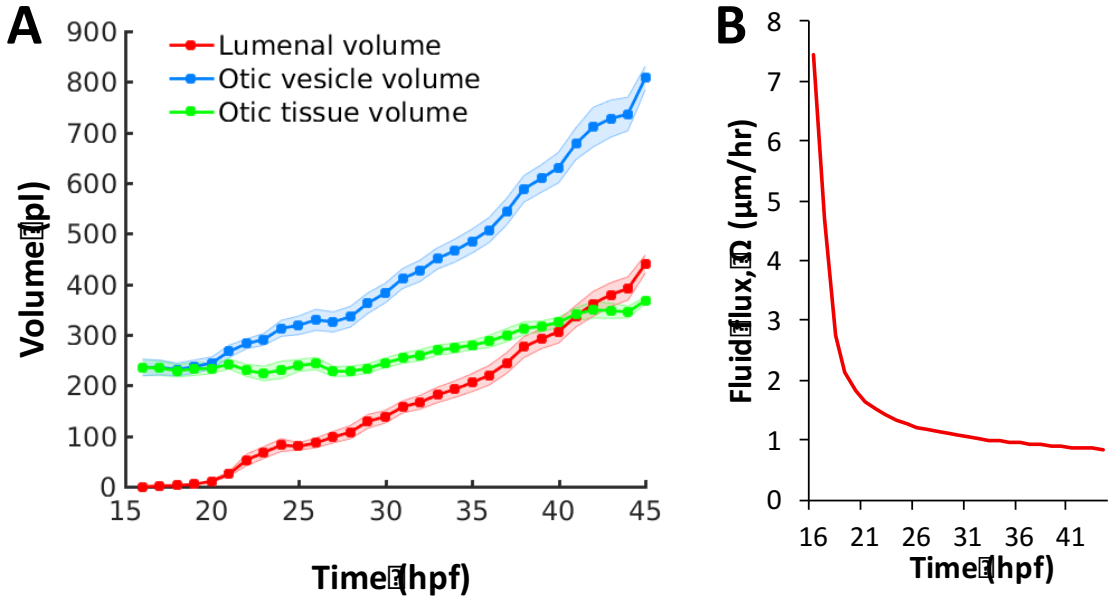

Figure 4. Growth of the otic vesicle between 16-45 hpf

(A) Quantification of vesicle (blue markers), lumenal (red markers), and tissue volumes (green markers). (B) Numerical calculation of fluid flux as a function of time by fitting quadratic polynomials to volume and surface area data.

The volume of the otic vesicle increased dramatically, by 572 pl from 235±16 pl to 807±23 pl (Figure 4A, blue curve). The majority of the increase in size of the otic vesicle is due to an increase in lumen volume (Figure 4A, red curve) from 0 to 440±18 pl (77% of the total increase) while tissue growth contributed only 23% to the increase in size. By using population-averaged measurements of luminal volume and surface area throughout the period 21-45 hpf, flux was approximately constant ($1\mu m^3/(\mu m^2.hr)$ ~ 1µm/hr) (Figure 4B).

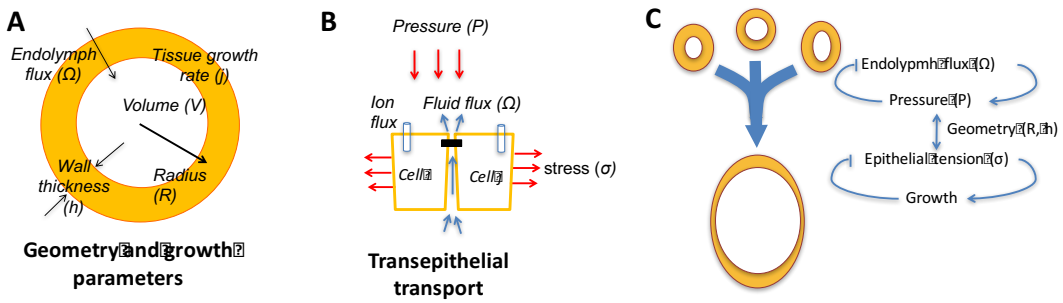

Figure 5. Schematic model of pressure and fluid transport in the inner ear

(A,B) Model relating vesicle geometry, growth rate, and fluid flux to pressure, tissue stress, and cell material properties. (C) Multiscale regulatory control of otic vesicle growth linking pressure to transepithelial transport.

As a result of fluid transport into the closed cavity, the development of hydrostatic pressure forces was identified using a novel ultrasensitive pressure probe (Figure 5A). Pressure stretched the tissue wall in a viscoelastic manner to physically deform otic cells and neighboring organs as they competed for physical space (Figure 5B). Perturbation of ion-channels (Na,K-ATPase) and pH blockers revealed the role of classical fluid transport mechanisms in generating the endolymph fluid. The work also examined whether pressure provided feedback to regulate otic vesicle growth by comparing growth in wildtype and punctured vesicles (no pressure). Interestingly, punctured otic vesicles had the maximum observed fluid flow rates per cell apical surface area (fluid flux). Fluid flux gradually decreased and reached wildtype homeostatic rates as pressure increased to its set-point when the otic vesicle regenerated to its true volume. Figure 5C summarizes the overall model of how otic vesicle growth rate is controlled by pressure negatively

regulating fluid transport. Thus, a major unanswered challenge then is how hydrostatic pressure is interpreted by physiological fluid transport mechanisms.

Fluid Transport Across an Epithelium

The phenomenon of transepithelial transport is a well-established mechanism for creating cavities and fluid-filled structures in a developing embryo, such as the blastocoel in mammals and amphibians, eyes, ears, heart, kidneys etc (Stern et al., 1985). The transport of salts and fluid across an epithelium can occur through a variety of mechanisms involving electrogenic pumps/transporters on cell membranes and aquaporins or through cell-cell junctions (Preston et al., 1992 and Hill & Shachar-Hill, 2006 and Fischbarg, 2010). Two classes have been identified: (1) Tight epithelia whose intercellular junctions are tight and present low permeability for movement of water. In such epithelia, water transport is driven exclusively in the presence of a concentration gradient across the cell's apico-basal membranes, through transcellular osmosis across cell membranes in series, and by traversing of aquaporins present. Examples of such epithelia studied in literature are the kidney collecting duct and the cultured Madin-Darby canine kidney (MDCK) cell layers. (2) "Leaky" epithelia include those that transfer fluid in the absence of an external osmotic gradient and between solutions that are of similar osmolarity. Examples of such epithelial linings studied include the corneal endothelium, gallbladder, renal proximal tubule, exocrine gland, stomach lining, and small intestine among many others.

For leaky epithelia, two separate theories for explaining isotonic, paracellular transport have been proposed. The first mechano-osmotic theory identifies the role of aquaporins as osmotic sensors that couple cellular hypertonic flows with paracellular

hypotonic flows to produce a net isotonic flow at a cell (Hill & Shachar-Hill, 2006). The coupling is based on a hypothesized negative feedback mechanism from aquaporins to explicitly control tight junctions that set paracellular flow rates. The second electro-osmotic theory is based on the existence of recirculating currents that move ions and water through charged tight junctions (Fischbarg, 2010). Identifying the mechanism underlying fluid transport across an epithelium is an unresolved challenge in the field of epithelial cell biology.

Fluid Transport Mechanisms Identified in the Inner Ear

There is evidence suggesting that the isotonic transport of ions (actively) and water (passively) is responsible for the generation of endolymph fluid in the otic vesicle lumen. Back in the 1980's, Fernando Giraldez and colleagues conducted elegant electrophysiology experiments in the chick to measure transepithelial potential and resistance of the chick otic epithelium (Represa et al., 1986 and Giraldez et al., 1987). The results showed that (i) otic vesicles produce spontaneous transmural potentials of 4 mV (inner positive) and transmural resistance of 80 Ω/cm2 and (ii) the potential is affected by the composition of the bathing solution. These results suggested the leaky nature of the epithelia and the activity of ion transporters selectively moving ions across the interface. More recent studies on the development of blastocoele [58, 59], endoderm gut [60], spinal cord, and heart development [61, 62] have confirmed the role of transepithelial ion transport as a developmental mechanism regulating volume, pressure, or composition of closed extracellular spaces. For otic vesicle development in zebrafish, two articles have demonstrated this fact. (1) Blasiole and colleagues investigated the role of Na,K-ATPase genes in zebrafish ear development (Blasiole et al., 2003 and Blasiole et

al., 2008). They identified six isoforms of Na,K-ATPase genes that were differentially expressed during otic development and demonstrated that each isoform had a functionally distinct role (otolith formation, semicircular canal formation, etc.). They noted that antisense morpholino knockdown of Na,K-ATPase α1a1.1 expression blocked formation of otoliths due to reduced secretion of ions and that otic vesicles developed smaller volumes. This effect was phenocopied via treatment with ouabain, an inhibitor of Na,K-ATPase activity. (2) Whitfield and Abbas studied the zebrafish mutant little ears (lte) that displayed a spectrum of phenotypic anomalies: larva exhibited loss of endolymph volumes and swam in circles or upside down (Abbas & Whitfield, 2009). They linked this phenotype to mutations in sodium-potassium-chloride-cotransporter gene nkcc1.

Apart from the Na^+-K^+pump, the otic epithelium has also been shown to be enriched with ionic transporters such as the H^+-ATPases and Cl^-/$HCO3^-$exchangers for regulating pH homeostasis and maintaining membrane resting potential (Lang et al., 2007 and Couloigner et al., 2000 and Sterkers et al., 1984). More recent work has suggested examined whether intracellular fluids contributes to lumen expansion in the inner ear (Hoijman et al., 2015). Using timelapse confocal imaging, the authors find fluid volume loss in the epithelial cells by tracking individual cells in 3D+*time*. This occurs in concert with the expansion of the dorsoventral (DV) and mediolateral (ML) axes that raises the possibility of potential contribution of intracellular fluids to the endolymph volume growth. However, an intriguing question is how intracellular flows can generate such rapid growth and large volumes and whether perilymph plays a larger role.

Significance of Thesis

As a first step to linking the pressure feedback to fluid transport mechanisms in the zebrafish inner ear, this project focused on identifying the origin of endolymph fluid, the path taken, and the underlying biophysical mechanism. Two physical paths exist for the movement of fluid: (1) paracellular routes via intercellular junctions, or (2) transcellular routes across apical membranes. To identify the correct path, integrated approaches consisting of quantitative imaging with zebrafish embryos in combination with small-molecule tracer dyes, mathematical modeling of dye transport, and experimental perturbations were used.

Fluorescent tracer dyes were injected outside the vesicle and the movement of dye was recorded using high-resolution timelapse confocal microscopy. 3D image analysis was used to quantify the spatial localization patterns of the dye in paracellular, intracellular, apical, and basal regions. The established quantification pipeline generated datasets that linked transport dynamics to growth. The datasets suggest that dye movement occurs across basal junctions, through lateral spaces between cell membranes, and across apical cell-cell junctions (paracellular pores).

Using different mathematical models of transport, the coupling of movement of dye and fluid was examined to rule out the possibility that these two take two different paths. Two possibilities exist: (1) Fluid transport is coupled to dye transport (advective), and/or, (2) dye independently diffuses across apical junctions (diffusion transport). If fluid movement is coupled to dye movement, then dye transport should be proportional to the volumetric growth of luminal cavity. Any perturbation of fluid flow should also affect dye transport and vice-versa. Thus, by setting up mathematical equations for such

processes, fluid transport was perturbed to test model predictions to identify that dye was coupled with fluid movement (advective transport).

Chapter II.

Materials and Methods

The following section details the materials and techniques used throughout the study. A quantification pipeline was developed to generate datasets that linked transport dynamics to growth. Briefly, the movement of fluorescent tracer dyes was recorded using high-resolution timelapse confocal microscopy in the inner ear of zebrafish embryos. 3D image analysis was used to quantify the spatial localization patterns of the dye. Mathematical models were used to distinguish between different hypothesis and rule out those that do not explain data.

Zebrafish Strains and Maintenance

All fish are housed in fully equipped, regularly maintained, and inspected aquarium facilities. All fish related procedures were carried out with the approval of Institutional Animal Care and Use Committee (IACUC) at Harvard University under protocol 04877.The following fluorescent transgenic strains were used in this study: (i) nuclear-localized tomato and membrane-localized citrine (Tg(actb2:Hsa.H2B-tdTomato)hm25; Tg(actb2:mem- citrine)hm26), and (ii) Tg(actb1:GFP-utrCH)e116 for visualizing F-actin distribution (Behrndt et al., 2012).

Protocol for Embryo Mounting

Embryos were collected using natural spawning methods and the time of fertilization was recorded according to the single cell stage of each clutch. Embryos were incubated at 28 °C during imaging and all other times except room temperature during

injection and dechorionation steps. Staging was recorded using hours post-fertilization as a measure and aligned to the normal table (Kimmel et al., 1995). A canyon mount was cast in 1% agarose from a Lucite-plexiglass template and filled with 1X Dannieau buffer (Figure 6A,B). The template creates 3 linear-ridges of width 400 µm, depth of 1.5 mm, and length 5 mm. Embryos at 25-30-35 hpf stage were dechorionated using sharp tweezers (Dumont 55) and mounted dorsally or dorso-laterally into the immersed canyon mount with a stereoscope (Leica MZ12.5). Multiple embryos for concurrent imaging were mounted in arrays.

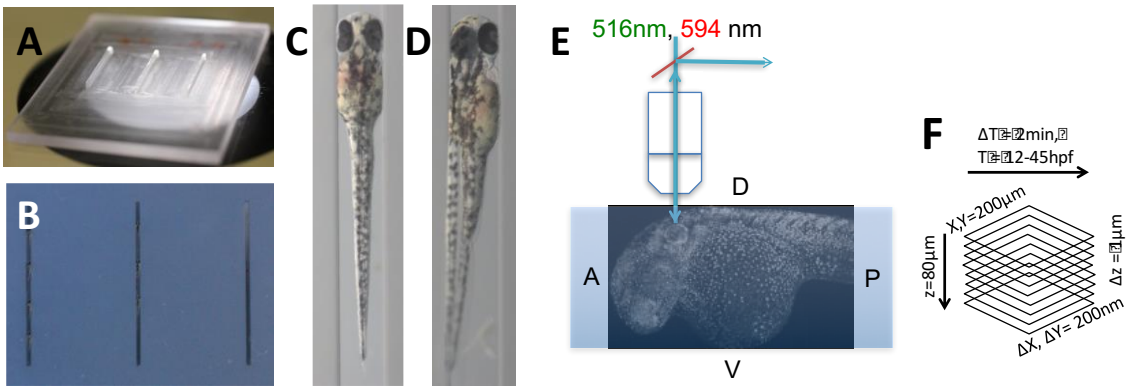

Figure 6. Confocal imaging of zebrafish inner ear growth

(A) A "canyon" template made of plexiglass with each canyon being 1.5 mm deep and 0.4 mm wide. (B) 1% agarose molds are cast using the template. Rows of zebrafish embryos from 16-45 hpf stages can be mounted in orientations that position the inner ear closest to the cover-slip for imaging. (C) Embryos are mounted in a dorsal orientation for imaging both ears simultaneously using a 20X, 1.0 NA objective. (D) Embryos are mounted in a dorsolateral orientation for obtaining higher-quality images (otic tissue depth along the path of light is minimized) using a 40X, 1.2 NA objective. (E) Transgenic zebrafish embryos expressing bright nuclear and membrane-specific fluorescent reporters are imaged using a confocal microscope in a time-lapse mode. Embryos are (Tg(actb2:Hsa.H2B-tdTomato)hm25; Tg(actb2:mem-citrine)hm26). (F) The acquired images typically cover a field-of-view of 200×200×80 µm. With a sampling of 0.2×0.2×1.0 µm, image dimensions are 1024×1024×80.

Protocol for Confocal Imaging

Live imaging was performed using a Zeiss 710 confocal microscope (objectives: Plan-Apochromat 20X 1.0 NA, C-Apochromat 40X 1.2 NA) with a home-made heating chamber maintaining 28◦C. For experiments requiring the imaging of both left and right ears in an embryo simultaneously, embryos were mounted dorsally (Figure 6B) and a Plan-Apochromat 20X 1.0 NA objective was used. The inner ear is situated closest to the embryo surface when viewed along the dorso-lateral axis. Dorso-lateral mounting permitted the imaging of the entire ear structure with the best resolution and minimizes the depth of imaging (Figure 6C). High-resolution imaging with a Plan-Apochromat 40X 1.2 NA objective facilitated the use of automated image analysis scripts for cell and lumen segmentation, and tracking the movement of fluorescent dyes. Laser wavelengths 488nm, 514nm, 561nm and 594nm lasers were used for confocal time-courses and other single Z-stacks. Embryos were immobilized by injecting 2.3 nl of 20ng/ µl α-bungarotoxin mRNA (paralytic) at the 1-cell stage for experiments requiring long-term time-lapse imaging (Swinburne et al., 2015).

Image settings vary by brightness of signal from maternal deposit. For example, (please see Figure 2): labels:membrane-citrine; lasers: 514nm (20mW, 3%); objective: lan-Apochromat 40X 1.2 NA at 1.0 zoom; pixel dwell time: 1.58 µs; pinhole size: 89 µm; line averaging: 1; image spacing: 0.2×0.2 µm, and 1024×1024 pixels per image, and with an interval of 1.0 µm through Z for 80 µm. The starting Z location for the embryo is ≈20 µm above the top of animal pole to allow sufficient space for it to stay in the field of view or sink in the agarose. Embryos were screened for their health before imaging.

Protocol for Dye Injection

To study the epithelial transport properties of the otic epithelium, 2.3 nl of fluorescent dye will be injected (Nanoinject) using a fine glass needle (15-25 µm diameter) into the cardiac chamber or directly into the otic luminal cavity (Figure 7). For injecting reliably, embryos between 25-45 hpf will be mounted dorso-laterally in the 1% agarose canyon mount. Embryos were anaesthetized at the 1-cell stage using 2.3 nl of 20ng/µl a-bungarotoxin mRNA. The dyes consists of 0.5 mM AlexFluor 594, 794 MW (Invitorogen) and Dextran, Texas Red; 3000 MW (Invitrogen). For short-term imaging of transport, confocal single slice imaging was used every 1 second for 10 minutes for each embryo. For long-term imaging of transport, embryos were injected at 30 hpf and a single Z-stack was collected after 5 hours of development at 35 hpf.

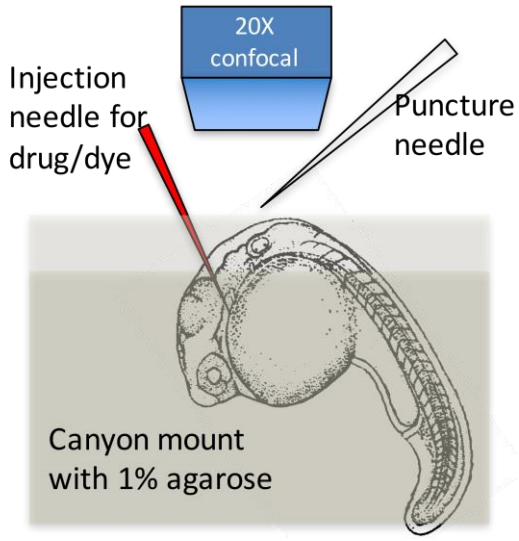

Figure 7. Vesicle Puncture and Injection Setup with Imaging

Embryos are mounted in a canyon mount made with 1% agarose for confocal imaging of left and right vesicles with a 20X objective. Drugs or dyes are injected into the cardiac chamber and get distributed rapidly throughout the embryo including the perilymph surrounding the ear.

Ouabain Treatment

In order to inhibit the activity of Na^+,K^+-ATPase, embryos at the 20 hpf stage were soaked in 1% DMSO + ouabain (Sigma Aldrich, CAS 11018-89-6) across a range of concentrations from 0-1 mM. Ouabain was stored at 10 mM in 1% DMSO and diluted to required concentrations in 1X Dannieau buffer before use. Ear size was assessed at 30 hpf as an endpoint. For long-term imaging, ouabain was added to 1% agarose mold used for mounting the embryos. To ensure consistent penetration, 2.3 nl of 0.75 mM ouabain was injected (Nanoject) into the cardiac chamber for circulation throughout the embryo. Assuming an average embryo volume of ~180 nl, this injected dose guarantees an effective concentration of 10 μM.

Puncturing of Otic Vesicle

To study the development of pressure in the otic vesicle, embryos were mounted dorso-laterally in a canyon mount (1% agarose by weight) with 1X Dannieau buffer and an unclipped glass needle was slowly inserted into the otic vesicle (Figure 7). The needle pierced the vesicle in a lateral direction. Puncturing locally affected epithelial connectivity, causing on average 1-2 otic cell and 1-2 ectodermal cell deaths. Luminal fluid (endolymph) leaked out along the circumference of the needle and the epithelium. Needles were positioned using a micromanipulator. The needle was later slowly withdrawn to study regeneration dynamics. Thereafter, the embryo was re-mounted in a dorsal orientation for imaging both the ears simultaneously.

2D/3D Image Analysis using GoFigure2

The entire quantification pipeline and scripts used are available online at: https://wiki.med.harvard.edu/SysBio/Megason/GoFigureImageAnalysis. The pipeline can be used for generating 3D surface reconstructions, automatic whole-cell and nuclei segmentations, and cell tracking. The code is open-source and written using the C++ programming language. After downloading, the code can be compiled in any platform using CMake, a tool for generating native Makefiles. The code is built by linking to pre-compiled open-source libraries, namely, ITK (http://www.itk.org) and VTK toolkit (http://www.vtk.org) for image analysis and visualization respectively. For visualization, the open-source and cross-platform GoFigure2 software was used. Measurements were analyzed and plotted with MATLAB (Mathworks) and Microsoft Excel.

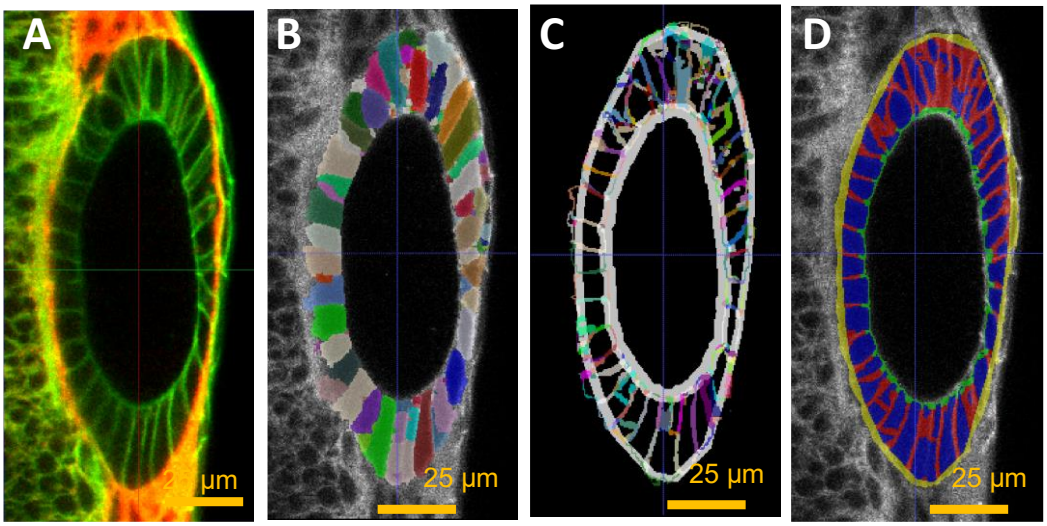

Figure 8. Automated image analysis to quantify dye localization pattern

The automated image analysis pipeline consists of using the (A) dye-injected image and then obtaining masks for (B) cell segmentations, (B) membrane segmentation, and (C) extraction of apical (green), basal (yellow), lateral (red) membranes and intracellular regions (red). Dye intensity patterns were averaged for each mask region to identify the localization patterns.

To obtain 3D models of the otic vesicles, 2D contours were first placed along regularly- sampled z-planes in GoFigure2 (Figure 3A). 3D reconstructions were obtained using the Powercrust reconstruction algorithm (Amenta et al., 2001) (https://github.com/krm15/Powercrust). Automatic cell and lumen-segmentation were performed using ACME software for whole-cell segmentations (Mosaliganti et al., 2012; Xiong et al., 2013) (Figure 3B-E). Apical, basal, and lateral membrane masks were extracted for each cell segmentation mask based on their distance from the 3D otic vesicle and luminal surface (Figure 8). The script ExtractMembraneSegmentations uses a distance threshold of 0.5 μm from otic vesicle and luminal surfaces to classify the apical and basal membranes respectively. The remaining membrane segments were classified as lateral membrane segments. The membrane masks were used to compute the localization of fluorescent reporters intracellular, paracellular, apical, and basal regions.

Modeling Dye Movement Across the Otic Epithelium

To investigate the path of fluid flow within the otic epithelium, a comprehensive mathematical theory was realized to account for all possible modes of dye transport into the otic lumen. The model was then tested against various experimental outcomes to evaluate the contribution of individual components. The model was then pruned and refined to explain the experimental results, and thus, clarify the relationship between dye transport and fluid flow.

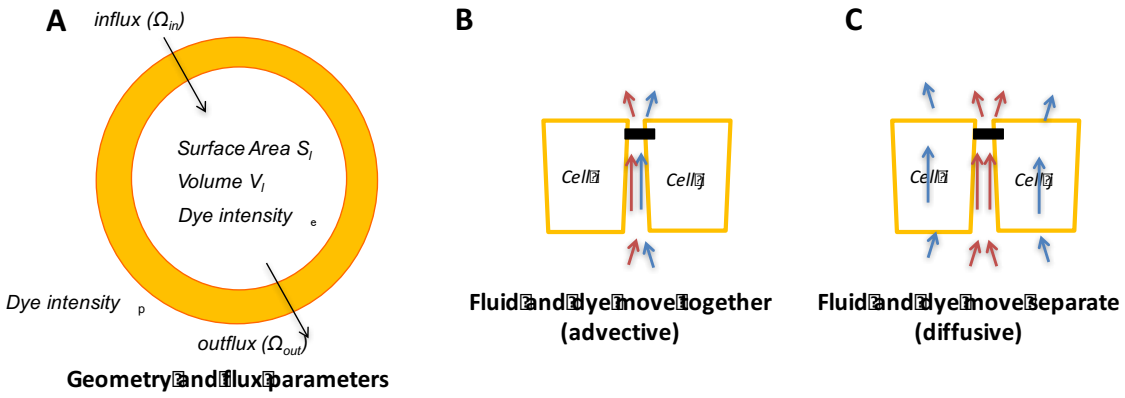

Figure 9. Schematic of the dye transport model

(A) Geometric representation of the otic vesicle as a spherical shell with volume V_l and surface area S_l. Influx and outflux of fluid is Ω_{in} and Ω_{out} respectively. (B) Dye and fluid move together through paracellular pores between lateral membranes. (C) Dye and fluid move through paracellular and transcellular routes separately.

Suppose, $\phi(x,t)$ denotes the concentration of the dye in space and time. The in-flux and out-flux from the luminal cavity is denoted as Ω_{in} and Ω_{out}, respectively. The total amount of fluorophore present in the lumen *F(t)*, as a function of time post-puncture, is given by:

$$F(t) = \int_{V_l} \phi(x,t)$$

There are two possible transport mechanisms that impact *F*:

1. Advective transport: This mechanism accounts for the passive movement of dye molecules due to bulk movement of fluid. Given the concentration in perilymph as ϕ_p and luminal concentration ($\phi_e = \frac{F}{V_l}$), fluid influx (δv_{in}) and outflux (δv_{out}) affect the total fluorophore present:

$$\Delta F = \phi_p . \Delta v_{in} - \phi_e . \Delta v_{out}$$

In the above Equation, fluid flow $\Delta v_{in} = S_l \Omega_{in} \Delta t$ and $\Delta v_{out} = S_l \Omega_{out} \Delta t$ respectively. Combining the two equations, we get:

$$\frac{dF}{dt} = \nu \phi_p S_l \Omega_{in} - \eta \frac{F}{V_l} S_l \Omega_{out}$$

Here, $\nu, \eta \in [0,1]$ denotes the permeability of otic tissue to the inward and outward movement of dye molecules respectively. Thus, the total fluorophore influx is the product of the perilymph concentration ϕ_p, luminal surface-area S_l, and fluid influx Ω_{in}. The total fluorophore outflux is the product of the luminal dye concentration $\frac{F}{V_l}$, luminal surface-area S_l, and fluid outflux Ω_{out}.

2. Diffusive transport across the perilymph-endolymph concentration gradient: Using Fick's laws of diffusion, the net dye flux, involving no movement of fluid, is proportional to the negative concentration gradient from the perilymph to endolymph. Therefore, the total fluorophore transport is scaled by luminal surface-area S_l and weighted by the diffusion coefficient *D* associated with the dye transport:

$$\frac{dF}{dt} = S_l D \frac{d\phi}{dx}$$

Integrating the contribution from all sources:

$$\frac{dF}{dt} = \nu \phi_p S_l \Omega_{in} - \eta \frac{F}{V_l} S_l \Omega_{out} + S_l D \frac{d\phi}{dx}$$

While this equation identifies the contribution of all sources, it is difficult to determine their individual contribution on account of several reasons:

1. Net fluid flux Ω is the difference between fluid in-flux and out-flux $\Omega = \Omega_{in} - \Omega_{out}$. Based on imaging measurements (Figure 4B), Ω was found to be a constant

throughout the otic vesicle growth phase (≈ 1μm/hr). However, the individual contributions of Ω_{in} and Ω_{out} are unknown.

2. The diffusion coefficient *D* depends on the size, charge, and structure of the fluorophore molecule and how that affects its transport through charged junctions and paracellular pores. Through development, junctional structure is also gradually modified to enhance its selectivity to the transport of small ions and water, a process necessary for ear function.

3. Estimation of the total fluorescence *F* and concentration in the lumen ($\phi_e = \frac{F}{V_l}$) is a coarse approximation due to imaging artifacts such as depth-dependent attenuation in intensity values and photobleaching of the fluorophore. Note that a significant portion of the lateral otic vesicle is embedded in brain tissue. Other factors include occlusion or shadows caused by the pair of otoliths.

4. Estimation of concentration in the perilymph ϕ_p is also a coarse approximation over long time-scales. Injection of tracer dye into the heart chamber/yolk results in a slow release, similar to a perfusion experiment. As a result, there is continuous accumulation of fluorophore in the perilymph mesenchyme. Thus, ϕ_p values change significantly through time. Furthermore, dye distribution in the perilymph region is non-homogenous and dependent on the presence of mesenchymal cells, vacuolar spaces, and extracellular material.

5. The gradient calculation ($\frac{d\phi}{dx} = \frac{(\phi_p - \phi_e)}{dx}$) in the diffusion term is unclear. Due to the aforementioned challenges in estimating $\phi_p$and ϕ_e, the numerator calculation is noisy ($d\phi$). Furthermore, the length of lateral spaces (dx) between otic cells (same as the wall thickness) is spatially non-uniform (Figure 1F).

6. The tissue permeability factors (ν, η) are unknown. These factors are possibly quite different from each other based on the charge selectivity of the tight junctions permitting the unidirectional transport of ions.

Chapter III.

Results

Otic epithelium is leaky and selectively permeable to tracer dyes

To address the path of water into the lumen, dye of low molecular weight (Alexa Fluor 594, 794 MW, negative charge) was injected into the cardiac chamber. Dye immediately accumulated into the fluid surrounding the inner ear (called as the perilymph) within 5 minutes and its transport into the lumen (endolymph) was recorded. This procedure ensured robust distribution of dye in the perilymph and prevented any otic tissue damage.

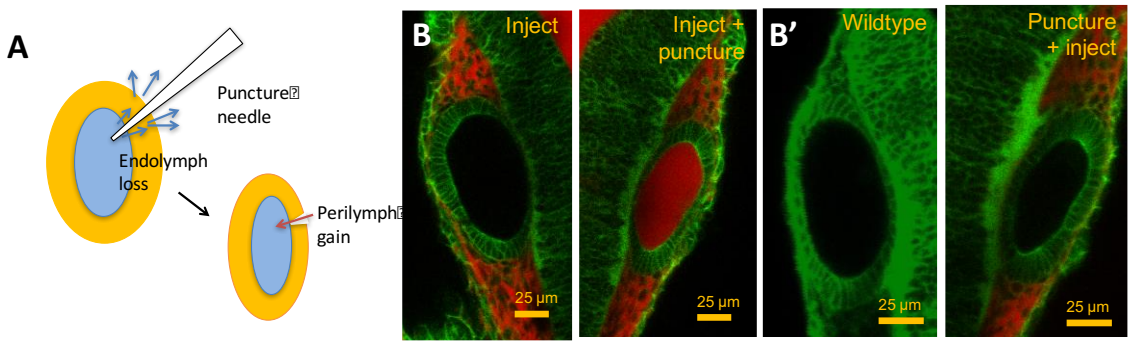

Figure 10. Otic epithelium heals rapidly post-puncture and forms a barrier to dye entry

(A) Schematic showing the route of lumenal fluid loss upon puncture and movement of dye from perilymph into the lumen. (B) 2.3 nl of 0.5 mM Alexa Fluor 594 tracer dye injected into the cardiac chamber at 30 hpf. The dye enters the circulation and is found to accumulate in the perilymph regions surrounding the vesicle. Puncturing of otic vesicle causes the dye to leak into the lumenal cavity. (B') Injection of dye five minutes post-puncture restricts dye transport to the perilymph, thus demonstrating the rapid sealing property of the otic tissue.

To ensure this approach was robust, the selectivity of the otic epithelium to dye transport was measured (Figure 10). When dye was injected and the otic epithelium punctured, dye immediately entered the luminal cavity and permeated the endolymph fluid (Figure 10B). However, when the otic epithelium was first punctured and allowed to heal for 5 minutes and then dye was injected, no movement of dye into the luminal cavity occurred. The proved that the otic epithelium presents a semi-permeable barrier to the dye. Thus, time-lapse imaging can be used to record the dynamics of dye transport to reveal the localization pattern, source, and path of fluid transport.

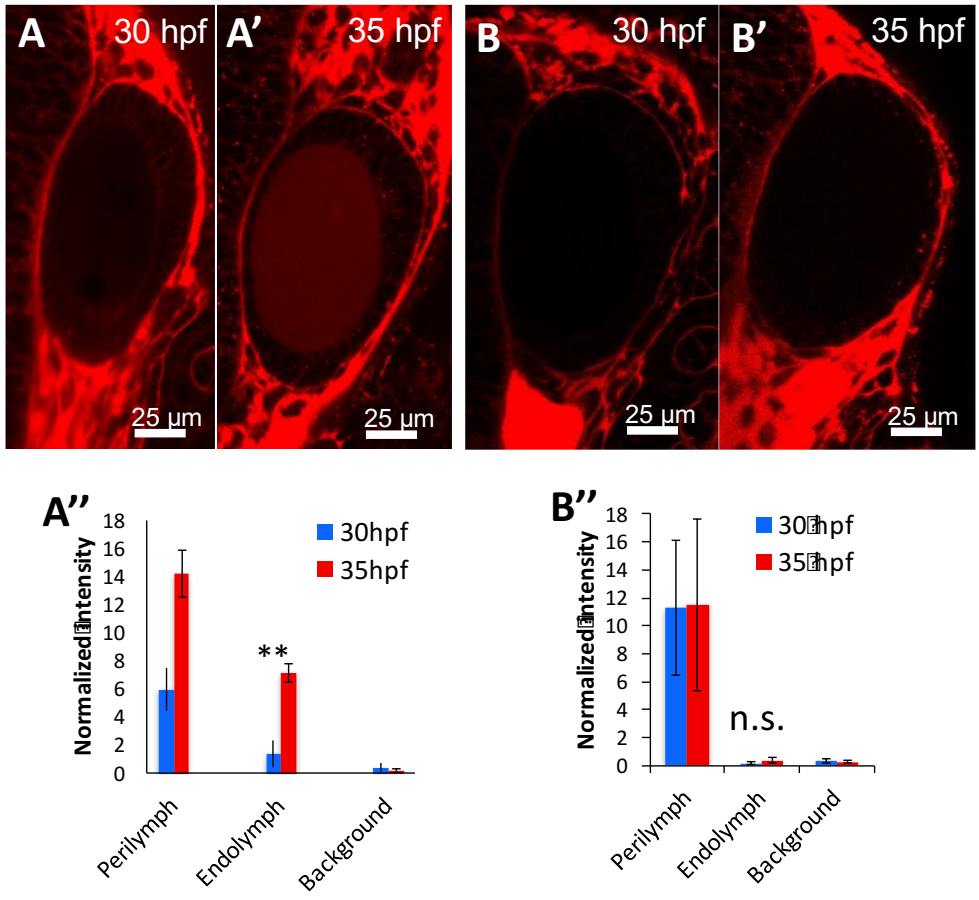

Figure 11. Otic epithelium is selective to the size of the tracer molecule

(A) Otic epithelium permeability to Alexa Fluor 594 transport is reduced or absent at 45 hpf. Dye movement into endolymph was tracked over 5 hours from (A) 45 hpf to (A') 50 hpf by measuring the change in lumenal intensity. (A'') Quantification of average lumenal dye intensity normalized to the confocal laser power used showed no significant increase. Error bars are SD (n=10).

Five hours after dye injection at 30 hpf, there is significant transport of Alexa Fluor 594 dye from the perilymph to the lumen (Figure 11A). This process was quantified in Figure 11A' where a significant increase in endolymph intensity was detected across these 5 hours. Note that perilymph concentration also increases since dye gradually circulates throughout the embryo before reaching the perilymph. So, the concentration gradually increases and saturates in time.

Otic epithelium is selective to dye molecular size

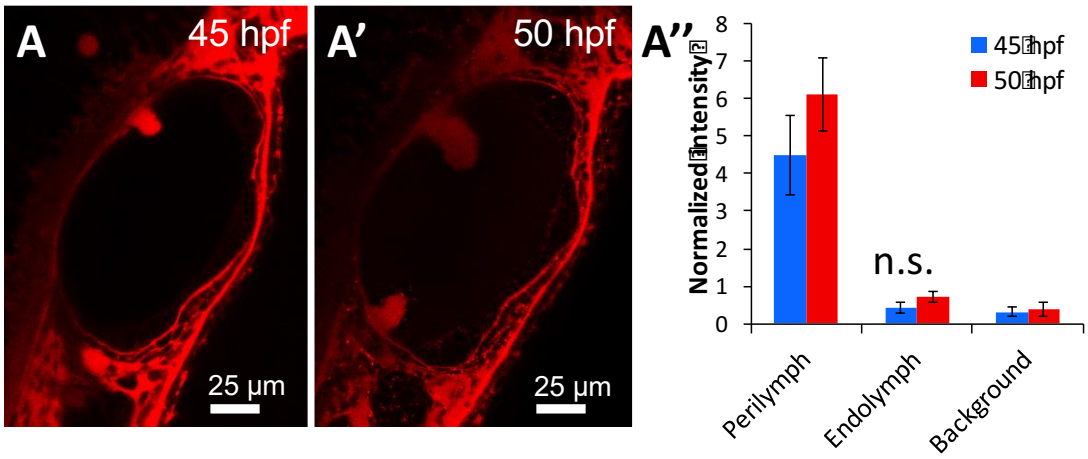

Figure 12. Otic epithelium changes into a tight epithelium around 45 hpf

(A) Otic epithelium permeability to Alexa Fluor 594 transport is reduced or absent at 45 hpf. Dye movement into endolymph was tracked over 5 hours from (A) 45 hpf to (A') 50 hpf by measuring the change in lumenal intensity. (A'') Quantification of average

lumenal dye intensity normalized to the confocal laser power used showed no significant increase. Error bars are SD (n=10).

In contrast, when the same experiment was conducted using a different dye Dextran Texas Red (3000MW, neutral charge), no significant accumulation of the dye in the endolymph occurred (Figure 11B-B'). Thus, these experiments reveal a size or charge-restriction by the otic epithelium in the movement of dye. The Alexa 594 dye was selected for use in all the subsequent experiments.

Otic epithelium transitions from a *leaky* to a tight epithelium at 45 hpf

To ensure that the otic epithelium presents a consistent barrier to dye transport through the growth phase, the experiment was repeated at other development times between 16-45 hpf. Dye transport is consistently present throughout vesicle growth 16-45 hpf (data not shown) but greatly diminished at the end of the growth phase at 45 hpf (Figure 12).

Growth dynamics are unaffected by the presence of dye

Since the dyes can potentially act as osmolytes or block paracellular pores, the volumetric growth rate of the otic vesicle in the presence of dyes was examined between 30-35 hpf. Dye was injected at 30 hpf in embryos and growth was compared to wildtype embryos. No significant differences in the volumes of the otic vesicle at 35 hpf was (Figure 13). Thus, this experiment further established that Alexa 594 dye is a potentially useful tracer for tracking fluid movement.

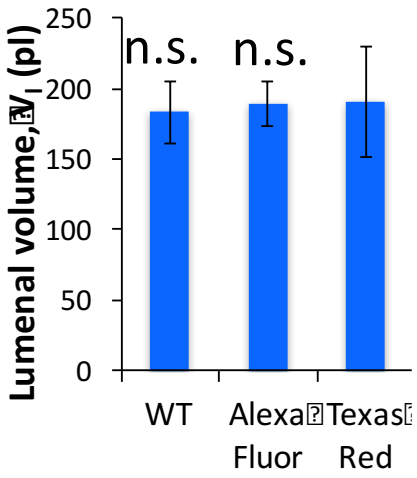

Figure 13. Growth unaltered with injection of dye tracer

Quantification of lumenal volume (V_l) at 35 hpf after dye injection at 30 hpf showed no significant differences in wild-type and injected embryos.

Lumenization involves the fusion of perilymph inclusions at apical tips of cells

Early lumenization begins at 16 hpf and ends at 18 hpf. At 16 hpf, cells secrete fluid from their apical surfaces to form a pair of lumen at the anterior and posterior closed ends of otic vesicle. With the gradual accumulation of endolymph, the lumens gradually connect over time to form a single connected lumen that looks like a dumbbell (Figure 14, 17 hpf). The otic vesicle then inflates by increasing its tissue mass, as well as by continuing secretion of endolymph. The lumen cavity expands in volume and becomes spherical eventually (Figure 2, 4). To track the initial formation of the lumen as the otic vesicle epithelializes, we used a cross of transgenic fish that had a membrane + actin highlighter. Membrane data allows one to use image analysis to accurately segment out individual cells and identify their apical, basal, and lateral membranes. Actin accumulates in the apical tips of cells and allows one to visualize the development of the lumen compartment.

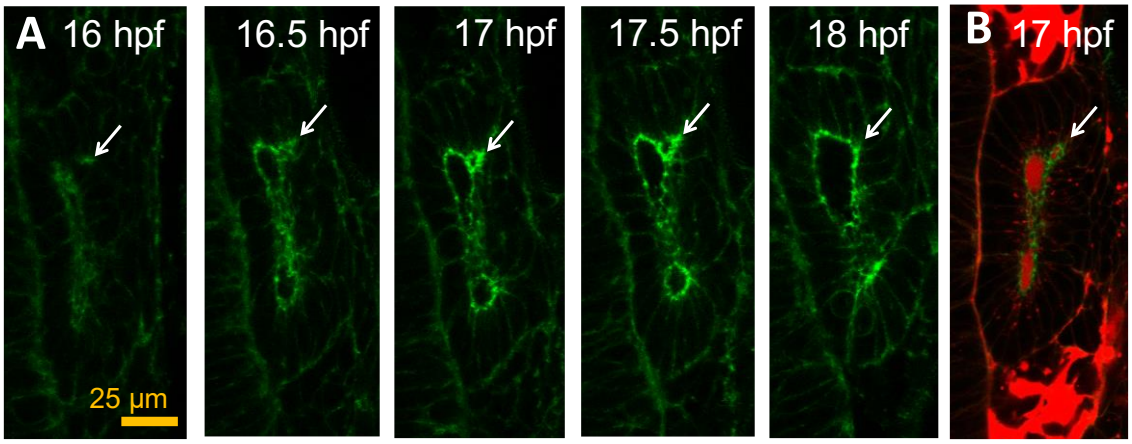

Figure 14. Lumenization involves the fusion of inclusions at apical tips of cells

(A) Lumenization involves fusion of multiple fluid compartments at the anterior-posterior poles. Temporal sequence (16-18 hpf) of confocal micrographs of a Tg(actb1:GFP-utrCH) embryo during lumenization. The white arrow shows the fusion of a fluid compartment at apical ends of intercalating cells with the larger lumenal fluid compartment. (B) Confocal micrograph with Alex Fluor 594 injection at 17 hpf showing the movement of tracer dye from the perilymph to the lumenal fluid compartment.

In some instances, the appearance and fusion of droplets with the main lumen was observed. In a special group of cells (white arrow in Figure 14A) that join the epithelium in a delayed manner, i.e., those cells at the fringe otic placode that intercalate to join the epithelium during the folding, they form a smaller lumen at their apical tips at a significant distance away from the main lumen. Lumenizing embryos were then injected with the Alexa Fluor 594 dye. Dye permeates the perilymph while the endolymph is excluded. However, the inclusion was found to be highlighted with the dye indicating that perilymph transport was involved in endolymph accumulation. This group of cells that intercalate late is highly-stereotyped and often only one such instance per embryo is spotted. For cells with apical surfaces already co-localized, the luminal fluid is continuously in contact with apical cell surfaces. Thus, for a majority of cells, finding

fusion events is not possible given that fluid secretion is continuous and below the diffraction-limit of microscopes to track movement of very small water droplets. The smaller lumens then fuse with the original lumen to form a single contiguous lumen.

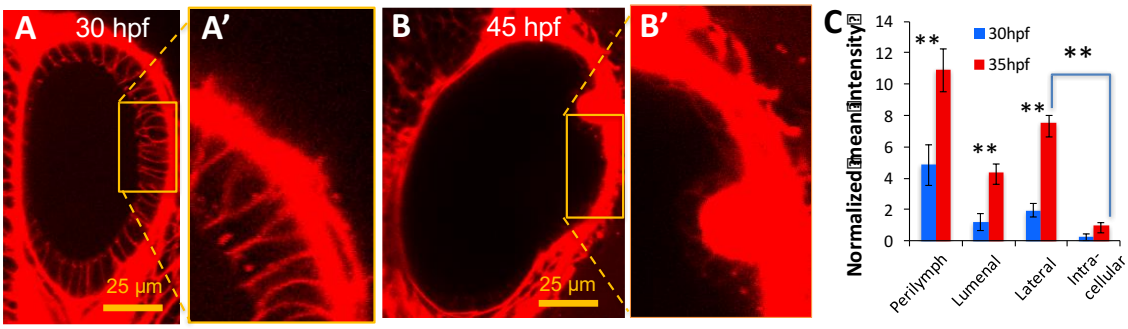

Figure 15. Paracellular dye localization pattern detected at 30 hpf but not at 45 hpf.

*(A-B) Dye injected into perilymph. Dye transport into lumen is detected at 30 hpf (B) but not 45 hpf. Dye movement is correlated with dye localization in lateral intercellular spaces (A', B'). Quantification of dye localization (C) shows a descending concentration gradient through the paracellular but not transcellular pathway. Error bars are SD. (n=10, * * p<5.0e-5).*

Dye localization patterns indicative of paracellular transport

To understand the path of the fluid flow, differences in dye localization patterns at 30 hpf when flux is high and 45 hpf when flux is low were examined. Transport at 30 hpf is correlated with dye localization to lateral membrane regions (Figure 15A-A'). The same lateral regions show low levels of dye localization at 45 hpf when transport is minimal (Figure 15B-B'). Using image analysis (Figure 8), the localization of the dye in intracellular, apical (lumenal), basal (perilymph), and lateral membrane locations was quantified. This evaluation was conducted across all the otic epithelial cells as dye was transported across a five-hour window (30-35 hpf). Dye was found to be predominantly

localized to the intercellular regions (between lateral membranes), which showed a marked increase in signal through time (Figure 15C). In contrast, intracellular regions did not register an increase in signal and had an overall low signal. High frame-rate imaging (1 frame/s) at 35 hpf showed boluses of dye that rapidly move from basal to apical between the lateral membranes of cells suggesting that dye and hence water are dynamically transiting between lateral membranes (Movie data not shown here). Together these data support that dye and possibly fluid movement is predominantly paracellular.

Experimental Validation Reveals Coupled Transport of Fluid and Dye

The transport equation developed in Chapter 2: Materials and Methods is as follows:

$$\frac{dF}{dt} = \nu\phi_p S_l \Omega_{in} - \eta \frac{F}{V_l} S_l \Omega_{out} + S_l D \frac{d\phi}{dx}$$

Given the significant challenges earlier identified in validating the parameters in this equation, three simple experiments were conducted whose outcomes provided insights into the contribution of individual terms.

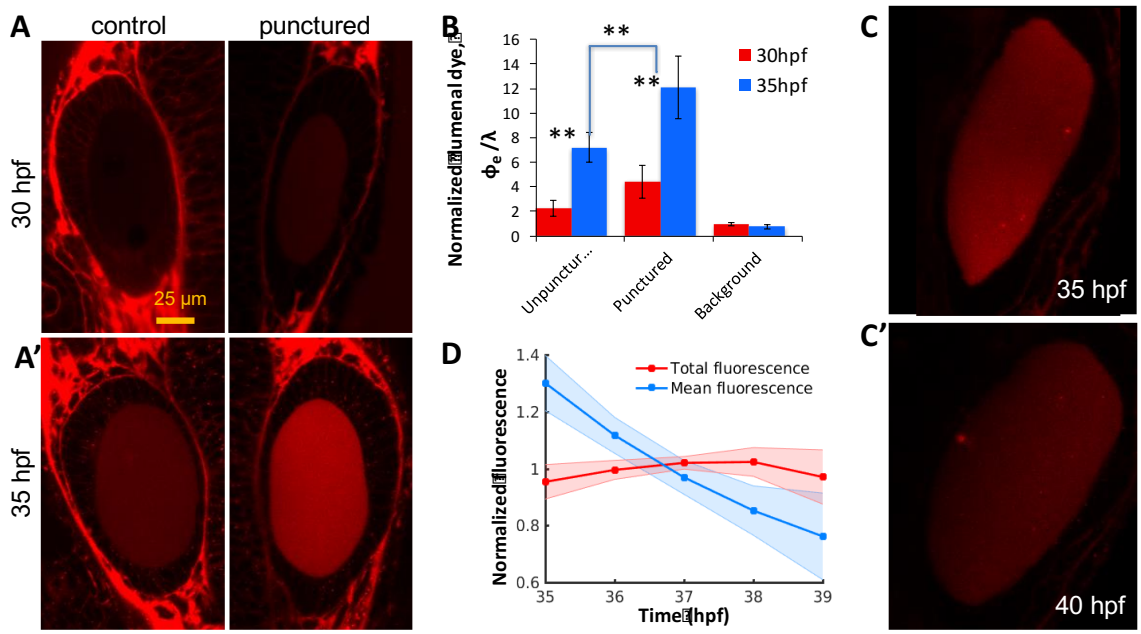

Figure 16. Dye transport is dependent on fluid influx and not on outflux

*(A) Dye injected into perilymph. Confocal micrographs showing higher flux of both dye and fluid into the lumen in the punctured than unpunctured vesicle in the same embryo over a 5 hour window starting at 30 hpf. (B) Quantification of mean dye intensity in the lumen (ϕ_e) in the unpunctured and punctured otic vesicle normalized by the laser power (λ) used. As a negative control, non-tissue background fluorescence is plotted (n=10, * * p<5.0e-5). (C-D) Dye injected into lumenal cavity. (C) Confocal micrographs showing dilution of dye in lumen during regeneration from 35 hpf to 40 hpf after puncture at 35 hpf. (D) Quantification of the total fluorescence (red curve) and mean intensity ϕ_e (blue curve) in the lumen across 35-40 hpf after dye injection at 35 hpf.*

Dye transport is dependent on fluid influx and not on outflux

To determine whether outward advective transport is important, 0.5 mM of AlexaFluor 594 dye was injected directly into otic vesicles and the total luminal expression was tracked over a period of time (Figure 16 C-C'). Previous experiments (Figure 4) identified that a five-hour endpoint after injection will involve sufficient volumetric growth of the otic vesicle to examine whether dye concentration dilution was

primarily due to perilymph inflow or also due to endolymph outflow. The rapid injection and needle withdrawal from the vesicle ensured that the temporal lag ($\approx 1 - 5$ seconds) between the initiation of injection and the actual fluid movement in the needle allowed the movement of only a small dye volume into the small otic vesicle. The experiment was conducted at the 35 hpf stage since the volume of unpunctured vesicles is sufficiently large (~200 pl) to accommodate extra dye fluid. To ensure that our initial measurements of total luminal fluorescence are not affected by any local tissue damage, a wait period of 15 minutes was incorporated before imaging the vesicle. Subsequently, z-stacks were collected every 1 hour, covering the entire otic vesicle. In Figure 16D, luminal intensity (blue curve) and total fluorescence (red curve) is plotted across the regeneration period. The mean intensity is found to rapidly decay on account of rapid volumetric growth from fluid regeneration. The total fluorescence is, however, a constant thereby proving that dye remains trapped inside the vesicle. Therefore, the transport equation is simplified by eliminating the outward transport term and substituting $\Omega = \Omega_{in}$.

$$\frac{dF}{dt} = \nu\phi_p S_l \Omega + S_l D \frac{d\phi}{dx}$$

Dye transport is advective and not diffusive

To differentiate advective transport from diffusion-related transport, fluid influx (Ω) was experimentally increased over wildtype values and the dye transport rate ($\frac{dF}{dt}$) was compared in both cases. Here, the contralateral ear was used as a negative control or wildtype. If the role of diffusion is significant, then less-than-proportional increase in dye transport compared to fluid influx (Ω) is expected. If not, dye transport is expected to proportionally increase with fluid influx. To increase fluid flux by 2-5X over normal

growth, otic vesicles were punctured at the 30 hpf stage and allowed for rapid regeneration of luminal volume (Figure 16A-A'). After puncture, tracer dye was injected into the heart chamber and transport into the lumen was tracked in punctured (Figure 16A-A', right) and contralateral unpunctured vesicles (Figure 16A-A', left, control). At the endpoint (35 hpf), unpunctured vesicles gained in intensity from advective dye transport related to normal growth (Figure 16 B). However, punctured vesicles, upon regenerating, had a significantly higher luminal intensity than unpunctured vesicles. Thus, this outcome suggests that a major contribution of dye concentration change in the endolymph is from inward advective transport than from diffusive transport.

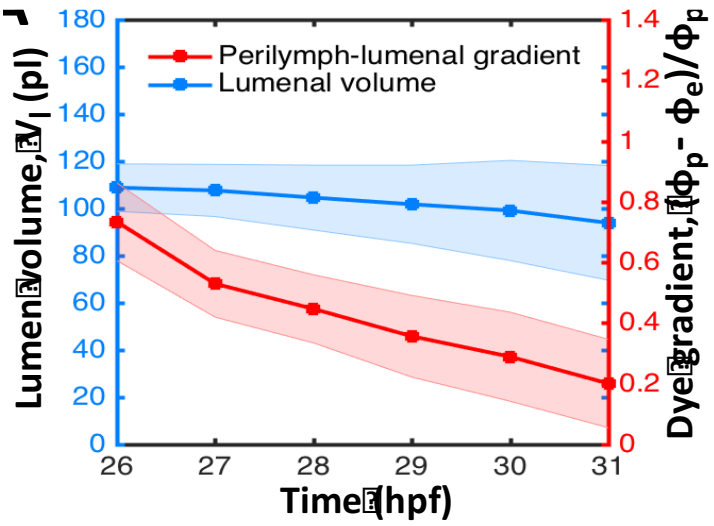

Figure 17. Dye transport is inhibited when growth is inhibited

Embryos at 25 hpf are injected with 2.3 nl of 1 mM ouabain. Dye is injected into perilymph. Quantification of lumenal volume V_l (blue) shows no growth. Concentration gradient of dye across otic vesicle is slowly lost (red).

Diffusive Dye transport is absent or not significant relative to growth

To determine the extent of diffusion-based dye transport, fluid influx was completely inhibited by administering 100 μM ouabain by injection in the yolk. In such embryos, two types of responses occurred where: (i) the embryos became unviable within 5 hours and vesicles lost endolymph volume from a disintegration of the otic epithelium, or, (ii) embryos appeared healthy for at least 5 hours and the otic vesicle volume remained constant (blue curve in Figure 17). In the first case, a reasonable explanation is that embryos became unviable due to a rapid release of the drug. In the second case, it is likely that the drug remained trapped in the yolk (at the injection site) and was released gradually over the observed period of 5 hours. In such embryos, changes in endolymph-perilymph intensity gradient was monitored and the equilibrium found to be established slowly over a 5 hour period (red curve in Figure 17). Thus, this experiment qualitatively supports our earlier result that advective transport is the significant contributor to overall dye transport.

Short-term Approximation of the Transport Equation

To overcome the challenges associated with quantifying parameters in the generalized transport equation, some simplifying approximations are used when evaluating transport in a short time-window. For a short time-window of imaging, the volume change (dV_l) is assumed to be negligible. Therefore, the rate of change of total fluorophore in endolymph is given by:

$$\frac{dF}{dt} = V_l \frac{d\phi_e}{dt} + \phi_e \frac{dV_l}{dt} \approx V_l \frac{d\phi_e}{dt}$$

Immediately after dye-injection, the concentration gradient $d\phi$ is the same as the perilymph concentration. Therefore, $d\phi = \phi_p - \phi_e \approx \phi_p$. The transport equation can then be simplified as follows:

$$V_l \frac{d\phi_e}{dt} \approx \nu \phi_p S_l \Omega + S_l D \frac{d\phi}{dx}$$

Under the assumption of spherical geometry of the otic vesicle, $\frac{S_l}{V_l} = \frac{1}{R}$.

Previously, the average radius of the otic vesicle $R(t)$ in wild-type embryos was quantified in Figure 4C). In addition, it was also shown that the growth rate dynamics are unaffected by the injection of the tracer dye (Figure 13). Therefore, the transport equation for short time-scales (in the order of minutes), immediately after dye-injection, with a spherical geometry, can be simplified as:

$$\frac{d}{dt} = \nu \frac{\phi_p \Omega}{R} + \frac{D}{\Delta x} \frac{\phi_p}{R}$$

$$= \frac{\phi_p}{R} (\nu \Omega + \frac{D}{\Delta x})$$

Thus, the model predicts a linear relationship between the rate of change in luminal dye concentration and the ratio of perilymph dye concentration to the luminal radius. To test this model, dye was injected into embryos at different developmental stages between 25-40hpf and measurements of ϕ were recorded as follows. To overcome photobleaching challenges, the medial z-plane of the otic vesicle was imaged in a timelapse mode for a short time-period of 10 minutes with a frame-rate of 1 frame/s. During this time, random motion of tracer molecules within the luminal fluid compensates for photobleaching in the imaging plane.

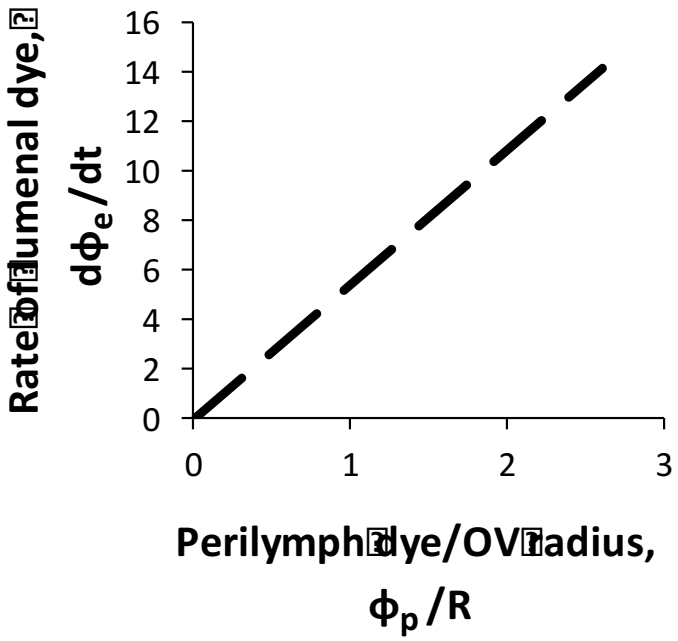

Figure 18. Rate of change of endolymph dye concentration is linearly correlated to the ratio of perilymph dye concentration and lumenal radius

Assuming dye transport is proportional to fluid transport predicts a linear correlation (black dashed line) between rate of change in lumenal dye intensity $\frac{d\phi_e}{dt}$ *in proportion to the ratio of perilymph intensity* ϕ_p *and vesicle radius R which closely matches experimental observations (blue marks). Error bars are SD.*

For short time imaging, a simplifying approximation was earlier evaluated as $\frac{dF}{dt} = V_l \frac{d\phi_e}{dt}$. An individual z-stack was also collected to measure volume V_l. For measuring average ϕ_p and ϕ_e, image analysis scripts were used to first develop a region of interest just inside the luminal or vesicle boundary and then averaged the values within those regions. Thus, this helped circumvent earlier mentioned problems, namely, depth-dependent attenuation and heterogenous distribution of dye.

Figure 18 plots the rate of change in luminal dye concentration ($\frac{d\phi_e}{dt}$) as a function $\frac{\phi_p}{R}$. Individual data points refer to individual embryos staged between 25-40 hpf and pooled together. The model prediction of a proportional linear relationship between these two quantities are validated by experimental observations, thus verifying the accuracy of the model.

Research Summary

To investigate the path of fluid flow within the otic epithelium, simple dye-tracing experiments were conducted by administering a fluorescent dye with a low molecular weight (Alexa Fluor 594, 794 MW, negative charge, Figure 10). Five hours after dye injection at 30 hpf, there is significant transport of dye from the perilymph to the lumen (Figure 11). Dye transport is consistently present throughout vesicle growth 16-45 hpf but greatly diminishes at the end of the growth phase at 45 hpf (Figure 12). Selective movement of Alexa Fluor 594 dye molecules but not Texas Red Dextran (3000 MW, neutral charge) suggests a size and/or a charge-restriction in the transport mechanism (Figure 11).

We also find evidence that small fluid droplets assemble between cells near the apical surface and fuse into the larger lumenal cavity (Figure 14). When dye was injected into the perilymph, the droplets also contain the dye. These data show that: (i) a single lumenal cavity forms by the fusion of apical fluid droplets, and, (ii) perilymph transport contributes to lumen formation and expansion throughout early growth.

Differences in dye localization patterns at 30 hpf when flux is high and 45 hpf when flux is low show that: (i) Lateral membrane spaces are highlighted at 30 hpf but not at 45 hpf, and, (ii) the epithelium changes from a leaky to a tight epithelium at the end of the growth phase (Figure 15). These results suggest a paracellular pathway to dye transport.

To determine if dye movement accurately tracks fluid flow, a mathematical model of lumenal dye transport was developed accounting for advective (pressure-driven, fluid-coupled) and diffusive inflows and outflows. Fluid flux was perturbed and compared experimental dye transport rates to theoretical predictions to gain insight into the contribution of the relevant mechanism. Lumenal dye transport is due to perilymph-to-lumen fluid transport (advective forward transport), diffusional transport, and/or lumen-to-perilymph fluid transport (advective reverse transport). By puncturing and following the regeneration resulting from increased fluid flux, we find that dye transport was proportional to perilymph-to-lumen fluid movement (Figure 16). Dye injected directly into a vesicle remained trapped-within over a 5 hour time-window (Figure 16) suggesting that fluid outflow was negligible or absent. In embryos where growth was abolished by ouabain treatment (Figure 17), perilymph to lumenal dye-concentration gradient was very gradually abolished by diffusion across a 5 hour time-period, thus demonstrating that diffusion harbors a limited role in dye transport. For advective forward-transport at short time-scales, our model predicts a linear relationship between lumenal dye concentration change and the ratio of perilymph concentration to vesicle radius. Using high frame-rate imaging and image analysis, we measured these quantities and observed an excellent agreement between model-predictions and experimental outcomes (Figure 18). Together,

these data show that dye flux accurately tracks bulk water flux, and thus, fluid moves from perilymph to endolymph via a paracellular path.

Chapter IV.

Discussion

In the adult ear, tight control of inner ear fluid pressure, volume and ionic composition is necessary to properly detect sound, balance, and body position. Pressure and fluid volume is also important to maintain the structural integrity of organs. Dysregulation of pressure-volume homeostasis can give rise to diseases including hypertension in the vasculature, Meniere's disease in the inner ear, glaucoma in the eye, and hydrocephalus in the brain. In the inner ear, this thesis presents evidence that luminal fluid flux occurs from paracellular transport mechanisms during early growth when fluid flux requirements are high and pressure works to inhibit these mechanisms. An open question is whether these mechanisms continue to contribute in later stages of development. Understanding how pressure feedback plays a role is relevant to all epithelia transporting fluid into closed cavities.

Pressure based feedback to control transport has been also observed in other tissues such as the dog intestinal mucosa (Hakim and Lifson, 1969), rabbit gall bladder (Hakim and Lifson, 1969; Eldrup et al., 1982), and the Necturus proximal tubule (Grandchamp and Boulpaep, 1974; Maunsbach and Boulpaep, 1983). Pressure may feedback into these mechanisms in several ways to regulate transport. Most generically, pressure creates a potential to drive fluid flux down the pressure gradient which will counteract opposing potentials of multiple types. Pressure may also act more specifically such as by affecting the conductance of ion channels or permeability of tight junctions. Interestingly, classical literature has shown that rising luminal pressure produces changes in the paracellular shunt ultrastructure and passive sodium ion back diffusion to impact

fluid transport in the Necturus proximal tubule (Grandchamp and Boulpaep, 1974; Maunsbach and Boulpaep, 1983).

Later in development, concurrent work in the Megason Lab, HMS has identified that a physical pressure relief valve is necessary for pressure-volume homeostasis in the inner ear (Swinburne et al., in review). Thus, together, these new insights on ear development and physiology will be critical to the development of effective clinical therapies for hearing and balance disorders, and for understanding size control in closed epithelial tissues.

Identifying the mechanism underlying fluid transport across an epithelium is an unresolved challenge in the field of epithelial cell biology. Direct visualization of fluid movement across junctions and cell surfaces is difficult to accomplish even with the latest state-of-the-art microscopes. Experiments which try to affect a transcellular pathway invariably have collateral effects on the paracellular pathway as well. This is because the many ion pumps, transporters, and aquaporin channels have multiple non-specific roles in both of these pathways.

In the zebrafish inner ear, this thesis using a novel approach to solve this problem. Although the presented results do not comprehensively rule out alternative models, they build a strong case for paracellular transport. The project focused on identifying the precise path by integrating high-resolution confocal imaging with small-molecule fluorescent dyes with a mathematical model of transport. Specific experiments were conducted that attempted to explain experimental outcomes using the model. Although some of the experiments were qualitative, they were helpful in ruling out alternative pathways and/or identifying the primary pathway. To account for technical challenges in

determining model parameters, the model was simplified using assumptions of spherical geometry, short time-window of imaging to eliminate photobleaching effects, and depth-dependent attenuation etc.

A recent article suggested that expansion of the lumen of the otic vesicle was in part due to loss of fluid from the cytoplasm of the cells in the otic vesicle resulting in their apparent thinning (Hoijman et al., 2015). The dye tracking experiments show that dye injected into the perilymph accumulates in the endolymph with no significant accumulation in the cytoplasm (Figure 15, 16). Previous work on volumetric growth dynamics (Figure 1) also shows that while the tissue volume remains flat, lumenal volume continues to increase. These observations suggest that cells are losing volume by cell division rather than by expelling fluid into the endolymph. These data suggest that fluid transport across the epithelium, rather than from inside cells, drives expansion of the otic vesicle.

Our model for vesicle transport integrates a range of geometry, shape, and fluid flow parmeters. By tailoring our model equations to different geometries and growth parameters, a unified mathematical framework can be realized to understand fluid transport in hollow organs including the eyes, brain, kidneys, vasculature, and heart. From a design standpoint, such a framework will facilitate an understanding of how individual transport mechanisms could compete or coordinate to achieve robust tissue morphogenesis and lead to investigations of how feedback works. Clearly, continuous one-way movement of fluid into a closed cavity is not physically possible. A mesoscale approach to modeling, such as the one presented in this work, connects quantitative cell-level behaviors up to more abstract physical processes in tissues and down to molecular

regulation to effectively elucidate the mechanisms of macroscopic traits (Savin et al., 2011; Shyer et al., 2013). In contrast, exclusively bottom-up approaches are often of limited utility in modeling macroscopic traits since many molecular details driving cell behavior are yet to be resolved (Megason et al., 2011).

The advantages of such a mesoscale model are several. First, a mesoscale model can be more easily applied to other contexts since the level of abstraction is higher making it less dependent on the specifics of the original context (fewer parameters). Second, growth kinetics and geometry parameters can be experimentally measured using in toto imaging approaches. New optical technologies for measuring tissue biophysical parameters such as stresses *in vivo* using oil droplets (Campas et al., 2014) and laser-ablation (Campinho et al., 2013; Hoijman et al., 2015), ionic gradients using fluorecent ionophores (Adams and Levin, 2012), and pressure (Link et al., 2004) via probes hold promise. And finally, the contribution of different molecular pathways in regulating model parameters can be prioritized for experimental investigation.

Bibliography

Abbas, L. and Whitfield, T. T. (2009). Nkcc1 (Slc12a2) is required for the regulation of endolymph volume in the otic vesicle and swim bladder volume in the zebrafish larva. *Development 136, 2837–2848.*

Amenta, N., Choi, S. and Kolluri, R. K. (2001). The power crust, unions of balls, and the medial axis transform. *Computational Geometry: Theory and Applications 19, 127–153.*

Bartel-Friedrich, S., & Wulke, C. (2007). Classification and diagnosis of ear malformations. *GMS Current Topics in Otorhinolaryngology, Head and Neck Surgery*, *6*.

Behrndt, M., Salbreux, G., Campinho, P., Hauschild, R., Oswald, F., Roensch, J., Grill, S. W. and Heisenberg, C.-P. (2012). Forces Driving Epithelial Spreading in Zebrafish Gastrulation. *Science 338, 257–260.*

Blasiole, B., Degrave, A., Canfield, V., Boehmler, W., Thisse, C., Thisse, B., Mohideen, M.-A. P. K. and Levenson, R. (2003). Differential expression of Na,K-ATPase alpha and beta subunit genes in the developing zebrafish inner ear. *Developmental Dynamics 228, 386–392.*

Blasiole, B., Canfield, V. A., Vollrath, M. A., Huss, D., Mohideen, M.-A. P. K., Dickman, J. D., Cheng, K. C., Fekete, D. M. and Levenson, R. (2006). Separate Na,K-ATPase genes are required for otolith formation and semicircular canal development in zebrafish. *Developmental Biology 294, 148–160.*

Brigande, J. V., Iten, L. E., and Fekete, D. M. (2000) A fate map of chick otic cup closure reveals lineage boundaries in the dorsal otocyst. *Developmental biology 227(2), 256–70*.

Centers for Disease Control and Prevention (CDC). Identifying infants with hearing loss - United States, 1999-2007. *MMWR Morb Mortal Wkly Rep. 59(8): 220-223*.

Vohr B. Overview: infants and children with hearing loss—part I. Ment Retard Dev Disabil Res Rev. 2003;9:62–64.

Collins T.J. (2007). ImageJ for microscopy. *BioTechniques, 43 (1):25–30.*

Couloigner, V.et al. (2000) Effect of locally applied drugs on the pH of luminal fluid in the en-dolymphatic sac of guinea pig. *American Journal of Physiology: Regulatory, integrative and comparative physiology 279, R1695–R1700*.

Diamond, J. M. and Bossert, W. H. (1967). Standing-gradient osmotic flow. A mechanism for coupling of water and solute transport in epithelia. The Journal of general physiology. 50(8): 2061–2083.

Schindelin J., Arganda-Carreras I., Frise E., Kaynig V., Longair M., Pietzsch T., Preibisch S., Rueden C., Saalfeld S., Schmid B., Tinevez JY, White D.J., Hartenstein V., Eliceiri K., Tomancak P., and Cardona A. (2012). Fiji: an open-source platform for biological-image analysis, *Nature Methods, 9(7): 676–682.*

Eldrup, E., Frederiksen, O., Møllgard, K. and Rostgaard, J. (1982). Effects of a small serosal hydrostatic pressure on sodium and water transport and morphology in rabbit gall-bladder. The Journal of Physiology 331, 67–85.

Eliceiri K.W., Berthold M.R., Goldberg I. G., Ibanez L., Manjunath B.S., Martone M.E., Murphy R.F., Peng H., A.L. Plant A.L., Roysam B., Stuurman N., Swedlow J.R., Tomancak P., and Carpenter A.E. (2012). Biological imaging software tools, Nature Methods, 9(7):697–710.

Fischbarg, J. (2010). Fluid transport across leaky epithelia: central role of the tight junction and supporting role of aquaporins. Physiological Reviews 90, 1271–1290.

Freter, S., Muta, Y., Mak, S.-S., Rinkwitz, S., and Ladher, R. K. (2008). Progressive restriction of otic fate: the role of FGF and Wnt in resolving inner ear potential. *Development 135(20), 3415–24*.

Gin, E., Tanaka, E. M. and Brusch, L. (2010). A model for cyst lumen expansion and size regulation via fluid secretion. *Journal of Theoretical Biology 264, 1077–1088.*

Giraldez, F., Represa, J. J., Borondo, L. and Barbosa, E. (1987). Polarization and density of Na-pumps in the inner ear of the chick embryo during early stages of development. *Development 100, 271–278.*

Grandchamp, A. and Boulpaep, E. L. (1974). Pressure Control of Sodium Reabsorption and Intercellular Backflux across Proximal Kidney Tubule. *Journal of Clinical Investigation 54, 69–82.*

Haddon, C. and Lewis, J. (1996). Early Ear Development in the Embryo of the Zebrafish, Danio rerio. *Journal of Comparative Neurology 365, 113–125.*

Hakim, A. and Lifson, N. (1969). Effects of pressure on water and solute transport by dog intestinal mucosa in vitro. *American Journal of Physiology 216, 276–284.*

Hoijman, E., Rubbini, D., Colombelli, J. and Alsina, B. (2015). Mitotic cell rounding and epithelial thinning regulate lumen growth and shape. *Nature Communications* 6.

Hill, A. E. and Shachar-Hill, B. (2006). A new approach to epithelial isotonic fluid transport: an osmosensor feedback model. *Journal of Membrane Biology* 210, 77–90.

Kil, S. H. and Collazo, A. (2001). Origins of inner ear sensory organs revealed by fate map and time-lapse analyses. *Developmental biology 233(2), 365–79*.

Kimmel, C. B., Ballard, W. W., Kimmel, S. R., Ullmann, B. and Schilling, T. F. (1995). Stages of embryonic development of the zebrafish. *Developmental Dynamics 203, 253–310.*

Lang, H. and Fekete, D. M. (2001). Lineage analysis in the chicken inner ear shows differences in clonal dispersion for epithelial, neuronal, and mesenchymal cells. *Developmental biology 234, 120–137*.

Lang, F., Vallon, V., Knipper, M. & Wangemann, P. (2007). Functional significance of channels and transporters expressed in the inner ear and kidney. American Journal of Physiology: Cell physiology 293, C1187–C1208.

McCarroll, M. N., Lewis, Z. R., Culbertson, M. D., Martin, B. L., Kimelman, D., and Nechiporuk, A. V. (2012). Graded levels of Pax2a and Pax8 regulate cell differentiation during sensory placode formation. *Development 139(15), 2740–2750*.

Maunsbach, A. and Boulpaep, E. (1983). Paracellular shunt ultrastructure and changes in fluid transport in Necturus proximal tubule. *Kidney International 24, 610–619.*

Megason, S. G. (2009). In toto imaging of embryogenesis with confocal time-lapse microscopy. *Methods In Molecular Biology Clifton NJ 546, 317–332.*

Megason, S. G., Srinivas, S., Dickinson, M. E. and Hadjantonakis, A.-K. (2011). Microscopy to mechanism across the scales of development: Editorial overview. *Current opinion in genetics & development 21, 519–522.*

Mosaliganti, K. R., Noche, R. R., Xiong, F., Swinburne, I. A. and Megason, S. G. (2012). ACME: Automated Cell Morphology Extractor for Comprehensive Reconstruction of Cell Membranes. *PLoS Computational Biology 8.*

Mosaliganti K., Swinburne IA, Obholzer N, Green AA, Tanksale S, Mahadevan, L, and Megason S. Size control of the the inner ear via hydraulic feedback. *In Review. 2017.*

NIDCD Epidemiology and Statistics Program: Statistics available at: https://www.nidcd.nih.gov/health/statistics/quick-statistics-hearing

Preston, G. M., Carroll, T. P., Guggino, W. B. & Agre, P. (1992). Appearance of water channels in Xenopus oocytes expressing red cell CHIP28 protein. Science256, 385–387.

Represa, J. J., Barbosa, E. and Giraldez, F. (1986). Electrical properties of the otic vesicle epithelium in the chick embryo. *Journal of Embryology and Experimental Morphology 97, 125–139.*

Rubashkin, A., Iserovich, P., Hernandez, J. A., and Fischbarg, J. (2005) Epithelial fluid transport: protruding macromolecules and space charges can bring about electro-osmotic coupling at the tight junctions. *The Journal of membrane biology. 208(3):251–263*.

Sanchez-Guardado, L. O., Puelles, L., and Hidalgo-Sanchez, M. (2014). Fate map of the chicken otic placode. *Development 141(11), 2302–12*.

Satoh, T. and Fekete, D. M. (2005). Clonal analysis of the relationships between mechanosensory cells and the neurons that innervate them in the chicken ear. *Development 132(7), 1687–97*.

Savin, T., Kurpios, N. A., Shyer, A. E., Florescu, P., Liang, H., Mahadevan, L. and Tabin, C. J. (2011). On the growth and form of the gut. Nature 476, 57–62.

Shyer, A. E., Tallinen, T., Nerurkar, N. L., Wei, Z., Gil, E. S., Kaplan, D. L., Tabin, C. J. and Mahadevan, L. (2013). Villification: how the gut gets its villi. Science (New York, N.Y.) 342, 212–8.

Stern, C. D., Manning, S. & Gillespie, J. I. (1985). Fluid transport across the epiblast of the early chick embryo. *Journal of Embryology and Experimental Morphology88, 365–384*.

Sterkers, O., Saumon, G., Tran Ba Huy, P., Ferrary, E. & Amiel, C. (1984). Electrochemical heterogeneity of the cochlear endolymph: effect of acetazolamide. American Journal of Physiology 246, F47–F53.

Swinburne, I. A., Mosaliganti, K. R., Green, A. A. and Megason, S. G. (2015). Improved Long-Term Imaging of Embryos with Genetically Encoded alpha-Bungarotoxin. PLoS ONE 10, e0134005.

Whitfield, T. T. Development of the inner ear. (2015). Current Opinion in Genetics & Development **32**, 112–118 (2015).

Wu, D. K. and Kelley, M. W. Molecular mechanisms of inner ear development. (2012). Cold Spring Harbor perspectives in biology **4**(8), a008409.

Xiong, F., Tentner, A. R., Huang, P., Gelas, A., Mosaliganti, K. R., Souhait, L., Rannou, N., Swinburne, I. A., Obholzer, N. D., Cowgill, P. D., Schier, A. F., and Megason, S. G. (2013). Specified neural progenitors sort to form sharp domains after noisy Shh signaling. *Cell **153**(3), 550–561.*

Yin, R. S. Z., Tang, P. H., & Tan, T. Y. (2011). Review of congenital inner ear abnormalities on CT temporal bone. *The British Journal of Radiology*, *84*(1005), 859–863.